ARMY RESEARCH LABORATORY

Electromagnetic Field Measurements Near a Single-Stage Reconnection Gun

by William O. Coburn and Calvin Le
Army Research Laboratory

Harry Martin
Department of Defense Joint Spectrum Center

ARL-MR-206

April 1995

The findings in this report are not to be construed as an official Department of the Army position unless so designated by other authorized documents.

Citation of manufacturer's or trade names does not constitute an official endorsement or approval of the use thereof.

Destroy this report when it is no longer needed. Do not return it to the originator.

REPORT DOCUMENTATION PAGE

Form Approved
OMB No. 0704-0188

1. AGENCY USE ONLY *(Leave blank)*	2. REPORT DATE	3. REPORT TYPE AND DATES COVERED
	April 1995	Progress, July–August 1994

4. TITLE AND SUBTITLE
Electromagnetic Field Measurements Near a Single-Stage Reconnection Gun

5. FUNDING NUMBERS
PE: 61102

6. AUTHOR(S)
William O. Coburn, Calvin Le (ARL), and Harry Martin (Department of Defense Joint Spectrum Center)

7. PERFORMING ORGANIZATION NAME(S) AND ADDRESS(ES)
U.S. Army Research Laboratory
Attn: AMSRL-WT-ND
2800 Powder Mill Road
Adelphi, MD 20783-1197

8. PERFORMING ORGANIZATION REPORT NUMBER
ARL-MR-206

9. SPONSORING/MONITORING AGENCY NAME(S) AND ADDRESS(ES)
U.S. Army Research Laboratory
2800 Powder Mill Road
Adelphi, MD 20783-1197

10. SPONSORING/MONITORING AGENCY REPORT NUMBER

11. SUPPLEMENTARY NOTES
AMS code: 611102.H430011
ARL PR: 4EE3E3

12a. DISTRIBUTION/AVAILABILITY STATEMENT
Approved for public release; distribution unlimited.

12b. DISTRIBUTION CODE

13. ABSTRACT *(Maximum 200 words)*

Electromagnetic (EM) field measurements were obtained near a single-stage reconnection gun accelerating a 194-gm, 4 × 4.5 × 1/4 in. aluminum plate. This type of EM launcher is of interest as an alternative for using explosive charges to launch a plate in the edge-on orientation. Electric and magnetic field measurements were designed to characterize the transient EM environment (EME) external to this capacitor-based EM launch system. The available data are included and selected data are discussed to illustrate the time history and spatial variation of the measured EME. The early-time EM fields associated with this system are directly related to the coil current, but under operational conditions there is a late-time electric field associated with the induced eddy currents in the plate. This report summarizes progress to date in characterizing this EME in terms of the relevant system parameters such as coil current and plate velocity.

14. SUBJECT TERMS	15. NUMBER OF PAGES
EM launch, EM fields	35
	16. PRICE CODE

17. SECURITY CLASSIFICATION OF REPORT	18. SECURITY CLASSIFICATION OF THIS PAGE	19. SECURITY CLASSIFICATION OF ABSTRACT	20. LIMITATION OF ABSTRACT
Unclassified	Unclassified	Unclassified	UL

NSN 7540-01-280-5500

Standard Form 298 (Rev. 2-89)
Prescribed by ANSI Std. Z39-18
298-102

Foreword

This report represents progress in ongoing research in the electromagnetic (EM) environment of various emerging systems. This is a joint program of the Nuclear and Directed Energy Division, the Weapons Concepts Division, and the Propulsion and Flight Division of the Army Research Laboratory Weapons Technology Directorate. Additional EM field measurements near reconnection guns are planned in 1995.

The results of this cooperative research program provide a technology base to address the EM environment effects (E^3) of advanced weapon concepts. The transfer of this technology to the Department of Defense Joint Spectrum Center, the E^3 community, and the Army RDECs should promote the development and use of emerging technologies in future military systems. One forum in this area is the EM Environment of Emerging Systems Working Group. Contact the authors for additional information on the annual working group meetings.

Contents

Figures

Appendix

1. Introduction

A capability to measure and predict the electromagnetic environment (EME) associated with emerging weapon concepts is required in order to address electromagnetic (EM) effects early in the design phase. Intense EM fields can be generated by EM launch systems, which typically contain a spectrum of frequencies from near dc to tens of kilohertz. Characterizing this EME is the first step in evaluating the EM effects on host vehicles, personnel, and electronic circuits. The EME associated with plate launch experiments was measured as the first phase of an Army Research Laboratory (ARL) research program in the EME of a plate launch system.

A reconnection gun [1,2] induces current in a conducting plate by the time-varying magnetic (H) field produced by an external launch coil. This type of EM launcher has no electrical contact with the plate and thus acts like a transformer. The time-varying current in the primary winding, the external launch coil, induces a current in the secondary winding, the plate [3,4]. The resulting Lorentz force, which launches the plate, has an equation of motion that can be derived from the total energy of the electrical circuit and the kinetic energy of the plate [4]. A multistage reconnection gun has been used to accelerate a metal plate in an edge-on orientation to high velocities [2]. Due to size and weight considerations, a single-stage reconnection gun is of more interest for active protection systems [4].

This report summarizes progress in the empirical characterization of the EME associated with an experimental single-stage reconnection gun at ARL. The transient E- and H-field vector components were measured at well-defined locations in the vicinity of this EM launch system. These data are used to identify the dominant features of the EME. It is proposed that the induced plate current is the source of the late-time electric (E) field, which is observed only when the plate is launched. The experimental data tend to support this model but indicate additional research is required for a conclusive description of this phenomena. The coordinate system used for the EM field mapping is centered between the coils and has its origin at the center, as indicated by (0,0,0) in figure 1. The test point location for EM field measurements is defined in this coordinate system by its (x,y,z) coordinates, in centimeter, where the plate is launched along the x-axis.

2. Methodology

The test approach is to measure the vector components of the EM fields in the vicinity of this system under operational conditions. EM field sensors are placed at various locations around the system and oriented in such a way as to measure the vector components of the E- and H-fields. The capacitor-based power supply is roughly 0.2 m behind the launch coil, and measurements showed no obvious EM fields due to the power supply at the field points of interest. That is, the transients associated with the power supply are small compared to the EME of the coil. The EME characterized under laboratory conditions can then be scaled to operational size systems.

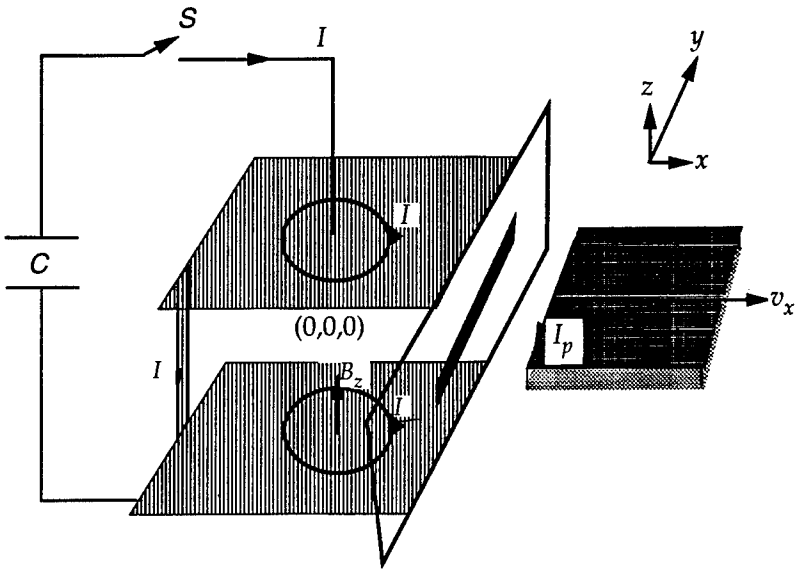

Figure 1. Coordinate system for plate launch experiments (not to scale).

Additional EM field mapping near this or larger scale active protection systems has not been possible so only preliminary results can be presented here.

2.1 Experimental Arrangement

A sub-scale, single-stage reconnection gun, accelerating a 194-gm 4 × 4.5 × ¼ in. aluminum plate, is used as a test bed for EM field measurements.* The single-stage reconnection gun is shown schematically in figure 1. It consists of two 5-turn coils machined from 6 × 6 × ½ in. copper plates, connected by a busbar, and separated by about 4 in. The power supply has a total capacitance of 1.7 mF (the capacitor, *C*, in fig. 1) discharged by an ignitron switch (the switch, *S*, in fig. 1) directly into the top coil. The coils are mechanically constrained by a 14 × 14 × 5 in. fiberglass structure, which is not shown.

The coordinate system origin is centered between the coils, which are 38.5 in. above the floor. Before launch, the plate is centered between and to the rear of the top and bottom coils. This launch coil is a variation of a previous design [4] that used a 9-turn helical coil with the plate positioned in the center. The external launch coil arrangement induces a current, I_p, in the plate due to the magnetic flux density, B_z, generated by the circulating coil current (see fig. 1). The resulting Lorentz force launches the plate with velocity v_x, which depends on the coil current, I. The ignitron switch is triggered at time $t = 0$ s, and the plate exits the launch coil after about 2 ms. The plate velocity is 48 m/s as measured with a photodetector array. It is stopped in a "catch box" at 15 ms after $t = 0$.

2.2 *H*-Field Sensors

The *H*-field sensors are multiple-turn loop antennas and, since all have air cores, the *B*-field, in Teslas, is related to the *H*-field (in A/m) by $\mu_0 = 4\pi \times$

**Provided by C. R. Hummer, U.S. Army Research Laboratory, AMSRL-WT-WD (July 1994).*

10^{-7} H/m. The sensors are 1000-turn multilayer coils of 18 AWG wire that respond to the *H*-field component normal to the plane of the coil [5]. The multilayer coil has an inside diameter of 4 in. and an outside diameter of 5 in. The sensor diameter is taken as 5 in. since it responds to the field cutting any turn of the coil. The sensor voltage is measured across a 3-Ω termination resistor, R_T, and R_L = 50 Ω, as shown in the equivalent circuit of figure 2. The voltage induced in this coil, V_{oc}, is directly related to the rate of change of magnetic flux cutting the loop area, *A*. Assuming the *H*-field, *H*, is constant over this area, the measured voltage, V_m, is

$$V_m = \frac{j\omega N\mu_0 HAR_{eq}}{R_a + j\omega L_a + R_{eq}} \approx \frac{N\mu_0 HAR_{eq}}{L_a} , \qquad (1)$$

where ω is radian frequency, μ_0 is permeability, N = 1000 turns, A = 0.013 m^2, and $R_{eq} \approx 3$ Ω is the combined load resistance. The antenna resistance and inductance can be readily calculated; for example, the calculated inductance of this multi-layer coil is 0.097 H. However, here the measured values, R_a = 8.6 Ω and L_a = 0.1 H, are used. The sensor transfer function is then about 2000 A/m/V (i.e., an antenna factor of 66 dB) and has a low-frequency rolloff according to equation (1). The measured sensor response is flat to within 3 dB from roughly 50 Hz to 50 kHz.

2.3 *E*-Field Sensors

E-field measurements were obtained using Stanford Research Institute (SRI) *E*-field sensors, which are a top-loaded monopole antenna design. The sensor uses a high-input-impedance amplifier, where dc power is supplied by a bias tee onto the coaxial signal cable. The combination termed E201 has a calibration factor of 2567 V/m/V (i.e., an antenna factor of 68 dB) and a bandwidth of 1 kHz to 200 MHz [6]. The measured antenna factor at 100 kHz is 65 dB, in reasonable agreement with Lee and Benwell [6]. The measured response as a function of frequency from 100 Hz to 100 kHz is shown in figure 3. Note that the high-frequency rolloff is that of the amplifier and the measured sensor response is flat to within 3 dB from 1.25 kHz to about 200 MHz.

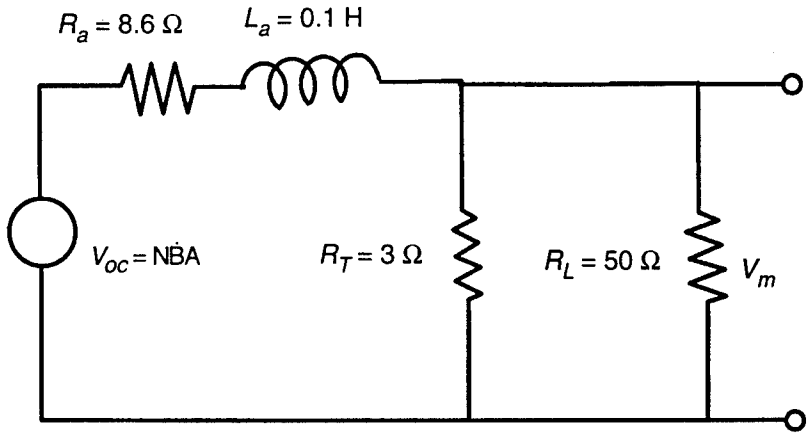

Figure 2. Equivalent circuit for magnetic field sensor.

E-field measurements with these sensors require frequency-domain correction factors for the probe response, which is done numerically in the Fourier transform space with the transient data obtained by Fourier inversion. Further calibration experiments in the laboratory showed that these sensors lose their directionality at low frequencies. That is, the sensor response to the field component normal to the monopole is only a few decibel less than the sensor response to the field component along the monopole. These sensors should be used with care at low frequencies. In these experiments an independent measure of the *E*-field is used to verify the data recorded from the SRI sensors.

Additional *E*-field measurements were obtained using wire antennas loaded by an external capacitance, C_L. The voltage across this load capacitor is measured using an active voltage probe [5]. The equivalent circuit is shown in figure 4 including the antenna capacitance, C_a, the antenna resistance, R_a, and the input impedance of the voltage probe, R_L. The induced antenna voltage, V_{oc}, is directly proportional to the *E*-field component along the antenna, E_0, and its effective length, h_e. However, h_e includes the length of the antenna element in addition to the length of metal before the high-impedance voltage probe tip (≈0.15 m). The measured voltage, V_m, is

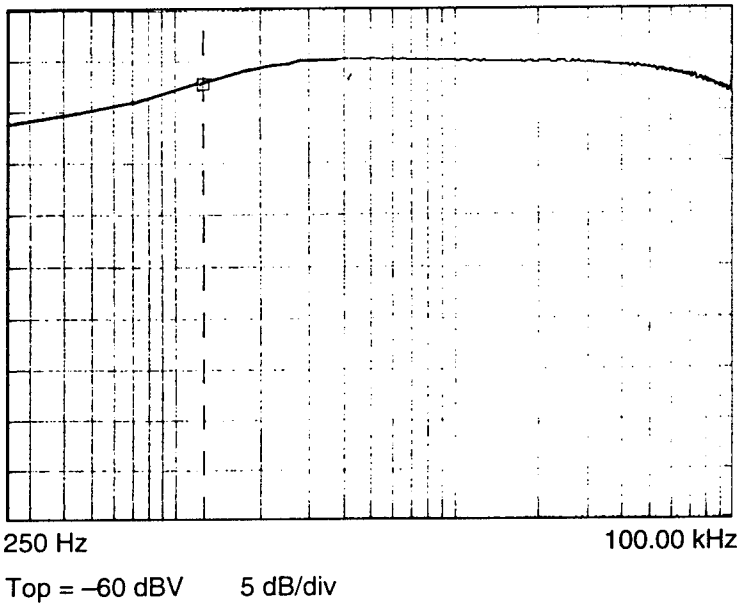

Figure 3. Measured SRI *E*-field sensor response.

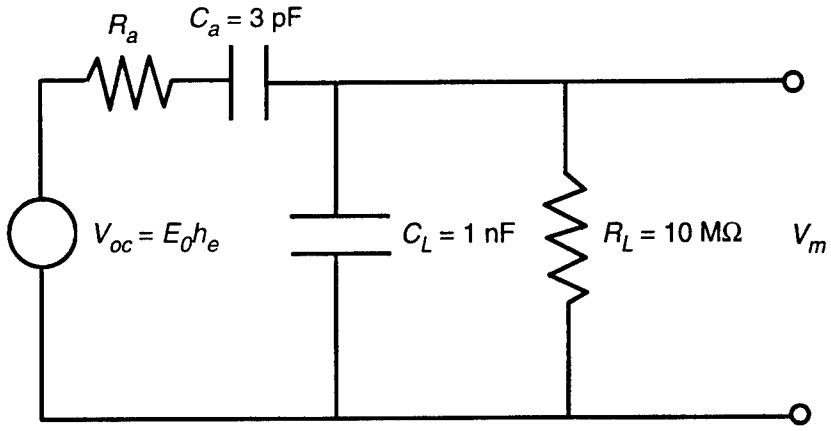

Figure 4. Equivalent circuit for electric field sensor.

$$V_m = \frac{E_0 h_e}{\left[R_a + \frac{1}{j\omega C_a}\right]\left[\frac{1}{R_L} + j\omega C_L\right] + 1} \approx \frac{E_0 h_e C_a}{C_L} \frac{\left[j\omega R_L C_L\right]}{\left[1 + j\omega R_L C_L\right]}, \quad (2)$$

where h_e = 0.20 m + 0.15 m = 0.35 m, C_L = 1 nF, C_a = 3 pF, R_L = 10 MΩ, and R_a, is negligible compared to R_L. The sensor transfer function is then 955 V/m/V (i.e., an antenna factor of 60 dB). This does not include the voltage probe gain, typically 0.1, so the calculated antenna factor for an 8 in. antenna element is 80 dB. The measured antenna factor at 100 kHz is 80 dB in close agreement with equation (2) and this response is flat to within 3 dB from 15 Hz to several megahertz. The sensor behaves as a high pass filter according to equation (2), as shown in figure 5 from 1 to 400 Hz. Note that the measured sensor response is contaminated by pickup noise from the electrical service, which is not present during the test series. The signal from these *E*-field sensors could be digitized but not permanently stored due to instrumentation incompatibilities. However, these sensors were used to qualitatively investigate the vector components of the late-time *E*-field and the measured data were consistent with the corrected data from the SRI sensors.

2.4 Test Conduct

The measurement instrumentation includes digital storage oscilloscopes, an analog oscilloscope with digitizing camera, PCs for control and data storage, and the various data acquisition components. The data are acquired through RG-223 double shielded coaxial cable. Data acquisition begins when the switch is triggered so that time t = 0 is when current begins to flow. In this test, series absolute timing information could thus be obtained and there were negligible shot-to-shot variations in both time and amplitude. The polarity of the measured signal is arbitrary and no attempt was made to maintain a consistent polarity for the acquired data. Although not shown, noise measurements under both background and

Figure 5. Measured probe response.

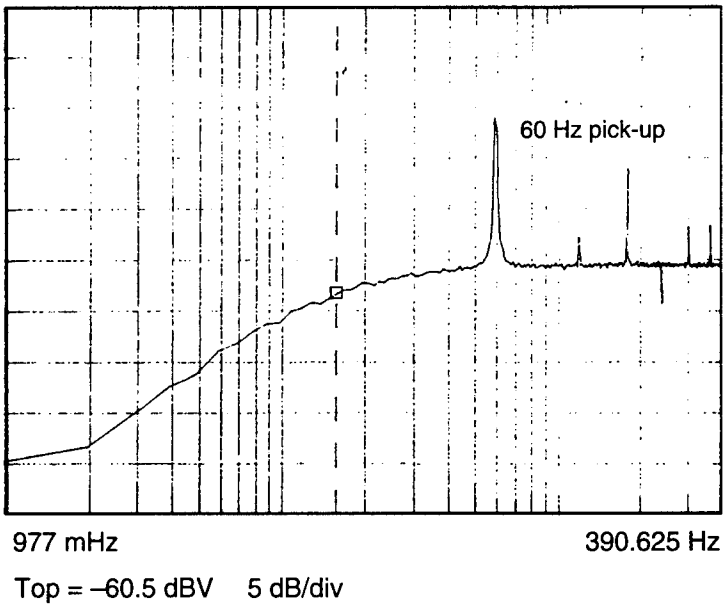

operational conditions verified a more than adequate signal-to-noise ratio for each measurement system and the absence of background noise. There are still small errors in the data acquisition and processing, where a conservative estimate for the end-to-end data acquisition error is ±10 percent. A conservative estimate for the error in probe placement is also ±10 percent, which leads to a total measurement error of about ±14 percent.

The test was designed to establish the EME generated under live-fire conditions, including any arcing or switching transients, and it consisted of 48 "shots." This system does not produce arcing under normal operations. The EME associated with the power supply is that of the switching transients, which were found to be negligible at the field points of interest. Three components of the *H*-field were measured at radial distances from 0.15 to 0.6 m at several locations along the flight path of the plate. *E*-field data were more limited due to instrumentation incompatibilities. However, sufficient data were obtained to demonstrate a near-static field associated with the launched plate. Measurements with and without the plate inserted into the launch coil were equivalent in early-time, but during plate launch a late-time signal was observed. This signal begins roughly when the plate exits the coil at 2 ms, it is bipolar, and it has features related to the plate velocity. Measurements with and without the system diagnostics and under various grounding and sensor configurations indicated that I_p was the source of this measured *E*-field. The majority of these data were not stored so this series of experiments is not presented here.

3. Results

The calculated coil current is shown in figure 6(a), which is a 2.2-kHz damped sinusoid. The peak amplitude is somewhat larger than the measured value of 92 kA, but otherwise accurately represents the measured coil current shown in figure 6(b). The electrical parameters of the launch coil circuit are $V_{coil} = 5$ kV, $L_{total} = 3$ μH, $C_{total} = 1.7$ mF, and $R_{total} = 8.5$ mΩ; these are kept constant throughout the test series. Since the magnetic flux,

$$\Phi = L_{total} I = \oint \vec{B} \cdot \hat{n} dA \approx B_z A_{coil} \ , \tag{3}$$

the field between the 6 × 6 in. coils without the plate is estimated as 11 T (8.75 MA/m). The field lines are actually concentrated between the plate and back edge of the launch coil, with distorted field lines in front of the plate [4]. Infrared photographs of the plate immediately after launch indicate that I_p is concentrated within about 20 mm of the side and trailing edges [4]. The available EM field data are shown in appendix A, excluding repeat and noise measurements, with selected data reproduced in the following sections. The signal polarity as shown is arbitrary, and the actual polarity of the EM fields can be inferred from the assumed direction of current flow in figure 1.

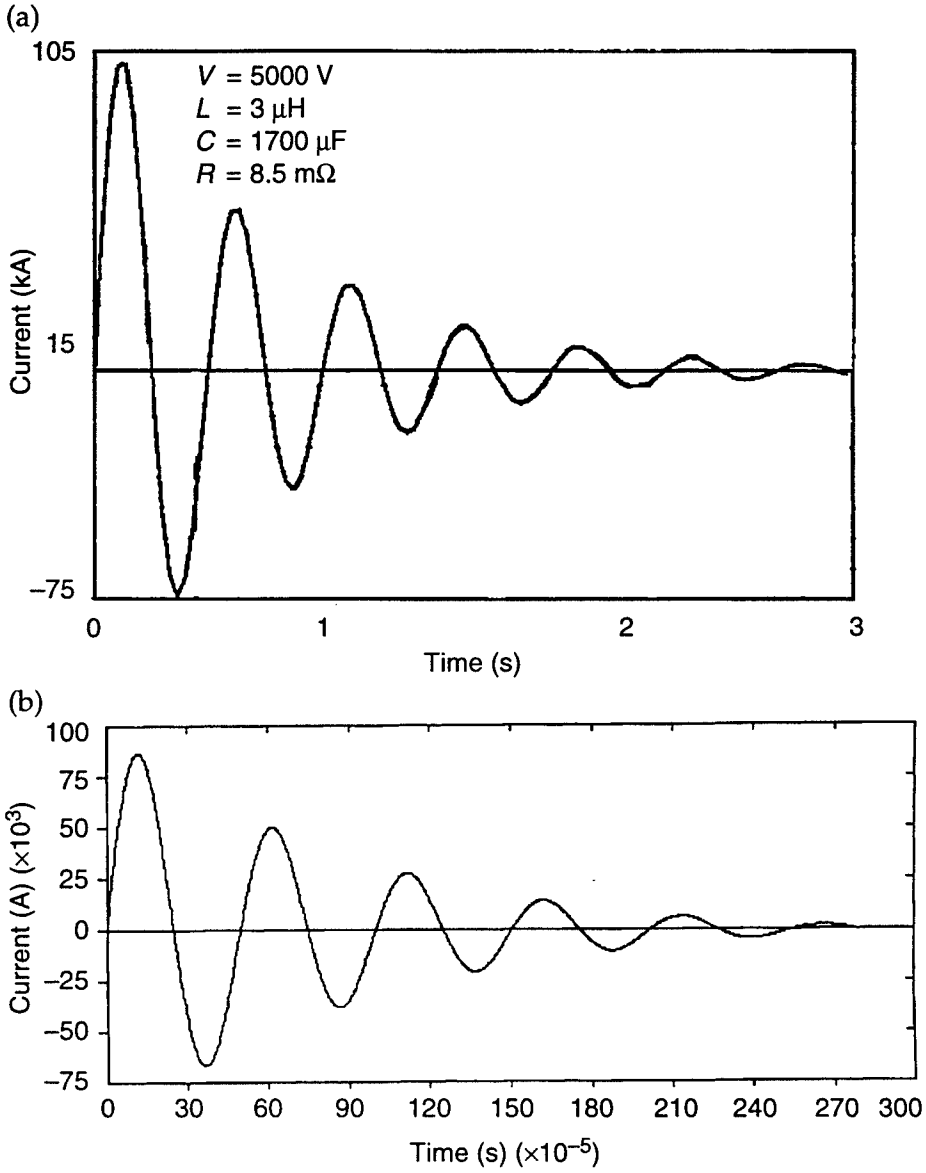

Figure 6. Coil current: (a) calculated and (b) measured.

3.1 *H*-Field

The *H*-field between the coils is in the z-direction (see fig. 1) or vertical with respect to the floor. There are azimuthal *H*-field components owing to *I* flowing in both the feed cable and the busbar that connects the top and bottom coils. The superposition of these field components near the launch coil determines the vector nature of the EME, which would include some shielding effect of the coils. At 2.2 kHz, the *H*-field shielding of ½ in.-thick copper (for a source to receiver distance of 10 cm) is about 92 dB [7]. At this frequency the top coil is equivalent to a solid copper plate. The measured H_z-field at (0,0,23), which is directly above the top coil, is shown in figure 7. This is the largest measured *H*-field component with a peak amplitude of 66 kA/m. The shielding of the top coil implies that the radiated field contribution from the bottom coil at location (0,0,23) is negligible. The calculated peak *H*-field at this location, for five concentric loops (radii of 0.75, 1.25, 1.75, 2.25, and 2.75 in.), each carrying 92 kA, is 78 kA/m. This estimate is in close agreement with the measured data in figure 7.

Figure 7. Measured H_z at location (0,0,23).

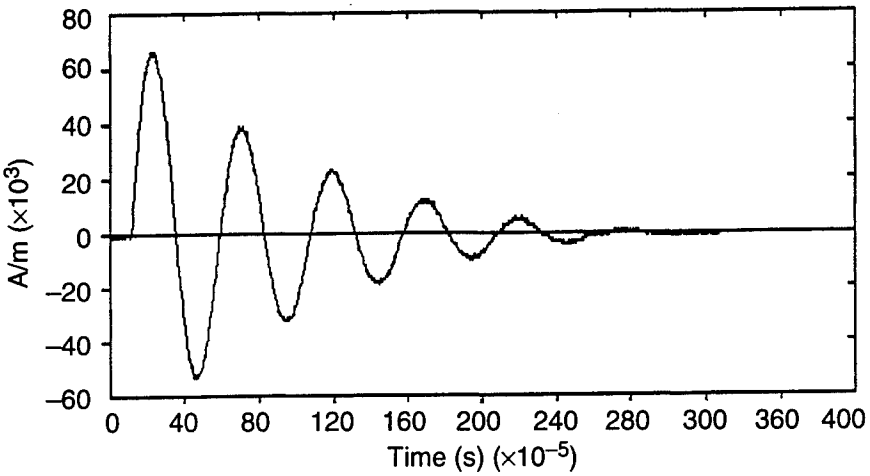

The H_z-field at (–8,8,8), which is toward the rear of the top coil, is shown in figure 8, where noise from the power supply is evident but small compared to the measured field. The measured H_z-field near the launch coil decays somewhat faster than $1/r^2$ from the origin, but this depends on the actual field distribution in the launch coil. An unusual behavior can be inferred from the measured H-field in front of the launch coil. The measured H_z-field at location (15,0,10) is shown in figure 9(a) and at location (15,0,28) in figure 9(b), where the field amplitude for this component further from the coil is larger. The other H-field components at these locations are shown in appendix A, where the y-components are roughly the same. The total H-field amplitude is reduced by a factor of 1.7 but 3.1 is the expected value. It seems then that the H-field in front of the launch coil decays inversely with distance and is dominated by the feed cable contribution. The data indicate that the vector nature of the H-field in front of the coil is complex and the spatial variation would depend on the fringing fields in front of the plate.

Measurements near the busbar connection (see fig. 1) were not practical because of the proximity of the power supply. The EME behind the launch coil would be the superposition of the vertical fringing field and the azimuthal field owing to I flowing in the vertical busbar. The feed cable contributes to the x- and y- (i.e., azimuthal) components of the total H-field, and this contribution dominates the EME at distances from the launch coil on the order of the top and bottom coil separation. The measured H_x- and H_y-fields at (0,–28,0) are shown in figures 10(a) and 10(b), respectively. The calculated azimuthal field at this location owing to the feed cable is 47.5 kA/m, where the measured peak amplitudes also combine to 47.5 kA/m. At these distances the feed cable contribution decays as $1/r^2$, as does the H_z-field from the launch coil. This is evident in the measured decay of the total H-field amplitude from location (0,–28,0) (see fig. A-4) to location (0,–56,0) (see fig. A-5), which is a factor of 4.3 compared to the expected value of 4. Comparison of the measured data at location (0,28,10) (see fig. A-3) and at location (0,–28,0) (see fig. A-4) shows that the H-field is roughly symmetric across the xz-plane, as would be expected. Symmetry across the other planes would be distorted according to the actual field distribution very near the launch coil. Note that there is no measurable (i.e., < 10 A/m) late-time H-field out to 32 ms and that all components of the measured H-field follow the coil current.

Figure 8. Measured H_z at location (–8,8,8).

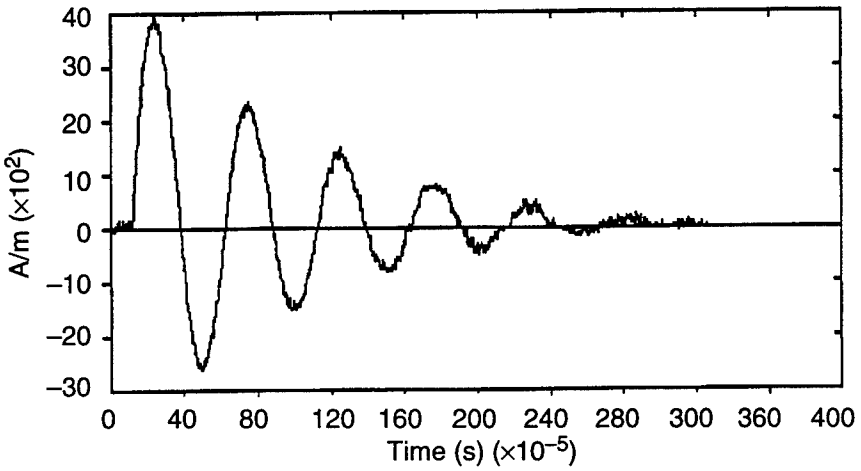

Figure 9. Measured H_z at locations (a) (15,0,10) and (b) (15,0,28).

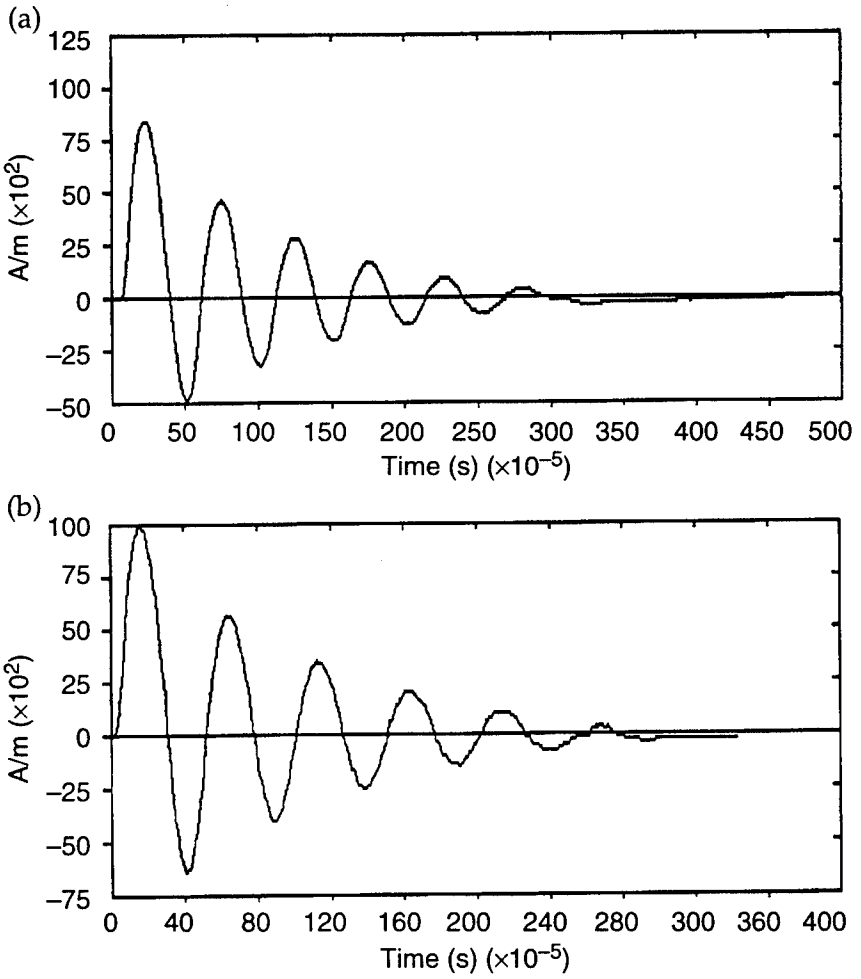

3.2 Early-Time *E*-Field

The early-time *E*-field also follows the coil current and decays inversely as the square of the distance from the coil. The measured decay of the total *E*-field amplitude from location (20,–28,10) (see fig. A-10) to location (20, –56,10) (see fig. A-11) is a factor of 2.86 compared to the expected value of 2.83. The measured E_y-field at location (20,–56,10) is shown in figure 11,

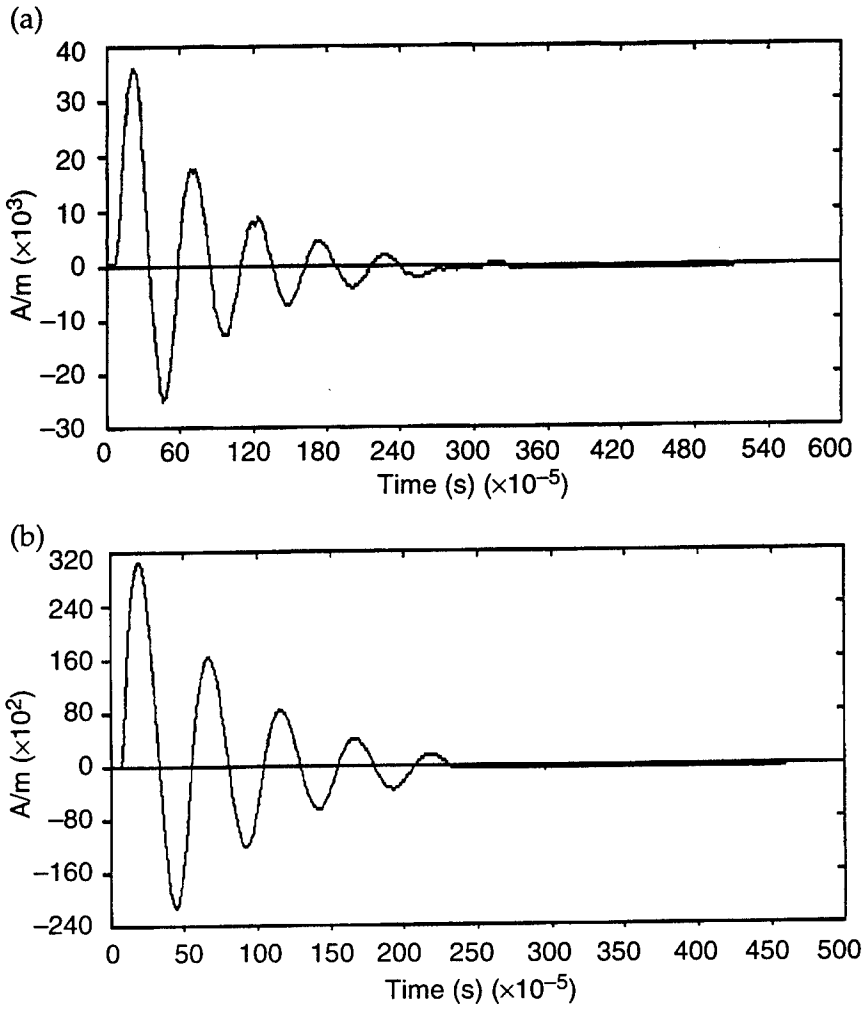

Figure 10. Measured (a) H_x at location (0,–28,0) and (b) H_y at location (0,–28,0).

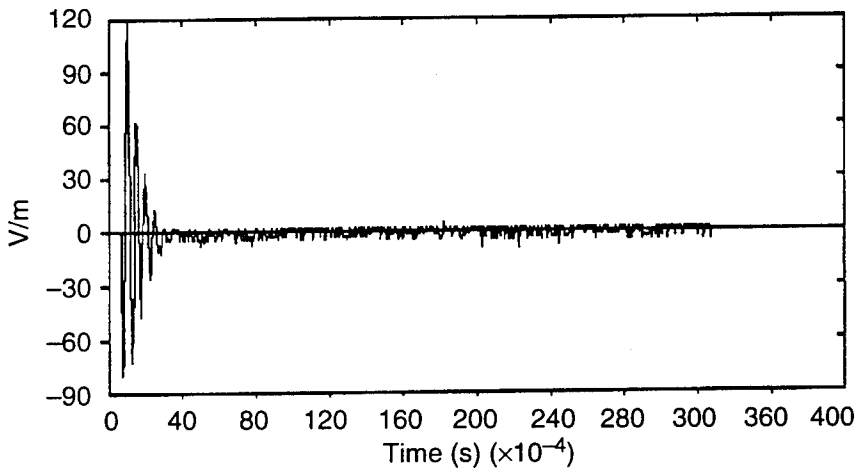

Figure 11. Measured E_y at location (20,–56,10).

where the noise level of the measurement system is on the order of 5 V/m. In comparison to figure 10(b), the wave impedance of the measured EME is about 19 mΩ at this location. That is, the launch coil represents a magnetic source where the measured wave impedance ranges from about 5 to 30 mΩ, depending on location. Note that there are no obvious noise contributions or switching transients associated with the power supply. The measured E_y-field at location (20,–28,10) is shown in figure 12, where now

Figure 12. Measured E_y at location (20,–28,10).

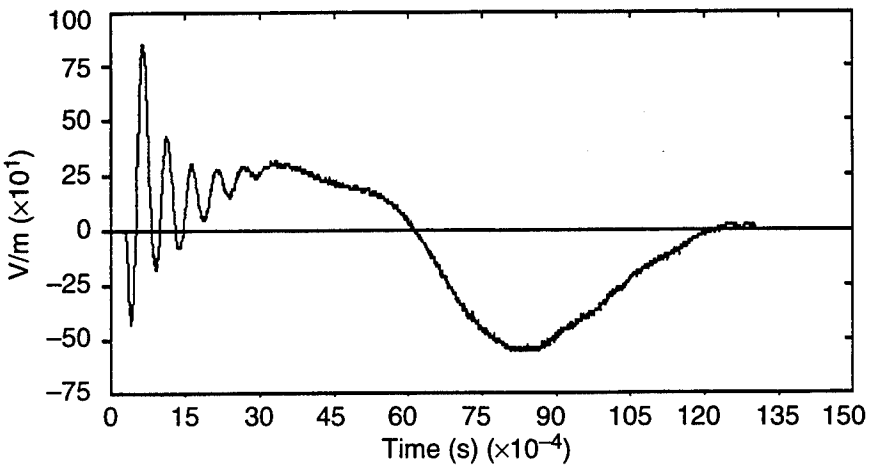

a late-time *E*-field signal is evident. This late-time signal disappeared when repeating this measurement without the plate inserted in the launch coil, while the early-time *E*-field remained unchanged.

3.3 Late-Time *E*-Field

The late-time *E*-field is difficult to measure because of the low-frequency rolloff of the SRI sensors (see fig. 3). This implies a larger measurement uncertainty in these data, but measurements with wire antennas (see fig. 5) confirmed the amplitude and transient characteristics of this late-time *E*-field. Although the SRI sensors have a derivative response at these frequencies, the data can be readily corrected. The transient characteristics of the corrected data are consistent with the wire antenna measurements. A bipolar signal where the second peak is always much larger than the first peak is evident whenever the test point location is sufficiently close to the plate fight path (i.e., the *x*-axis). It is proposed that this *E*-field represents a dipole contribution to the EME from the highly non-uniform induced eddy currents in the plate, which are smallest near the front edge of the plate and largest within 20 mm of the back edge. This current is primarily oriented in the *x*- and *y*-directions, but the *z*-component is not necessarily negligible.

The measured E_z-field at location (36,0,20) is shown in figure 13, where the late-time peak amplitude is 1.2 kV/m. The measured E_z-field at location (46,–18,0) is shown in figure 14, where the late-time peak amplitude has decayed by a factor of 1.7, but the location is a factor of 1.2 further from the origin. This signal, then, does not appear to decay as $1/r^2$ from the coil but rather as $1/r^3$ from the plate flight path. In this case, the expected reduction would be a factor of 1.5, in reasonable agreement with the measured value. Depending on the probe location, this late-time signal may be near the measurement noise level because of the decay with distance from the plate combined with the low-frequency rolloff of the SRI sensors.

As another example, consider the measured E_y-field at location (46,–8,5) shown in figure 15 and the measured E_y-field at (38,0,28) shown in figure 16. The measured reduction of the late-time peak amplitude is a factor of

Figure 13. Measured E_z at location (36,0,20).

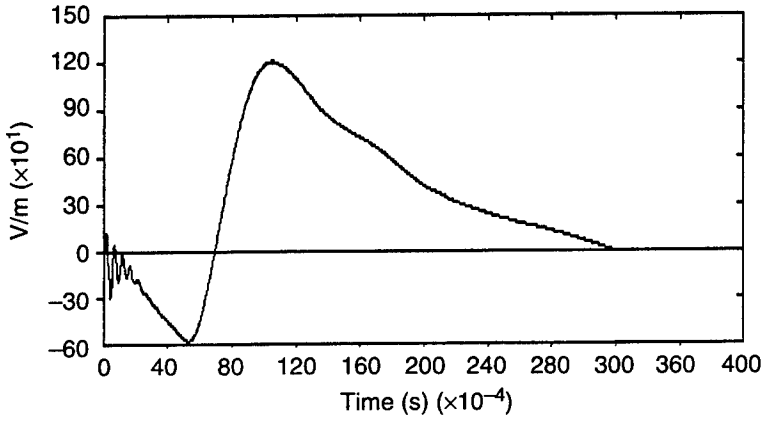

Figure 14. Measured E_z at location (46,–18,0).

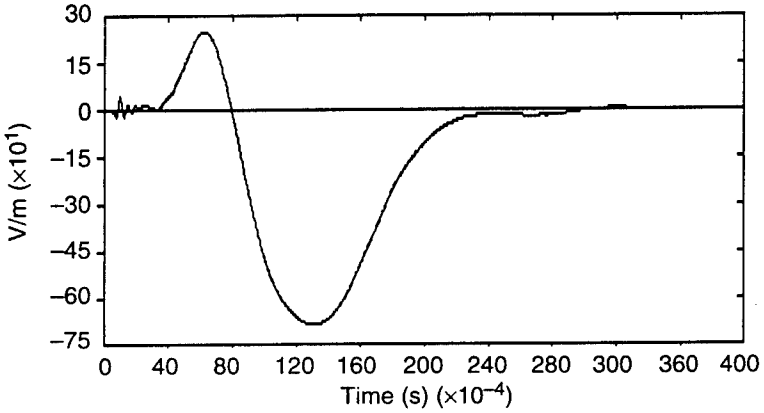

Figure 15. Measured E_y at location (46,–8,5).

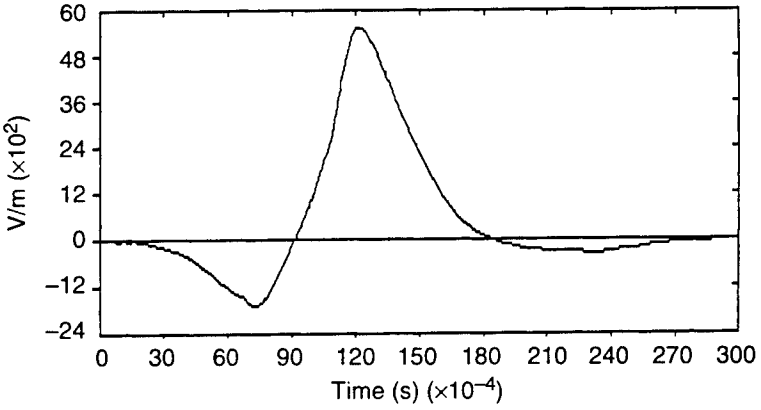

Figure 16. Measured E_y at location (38,0,28).

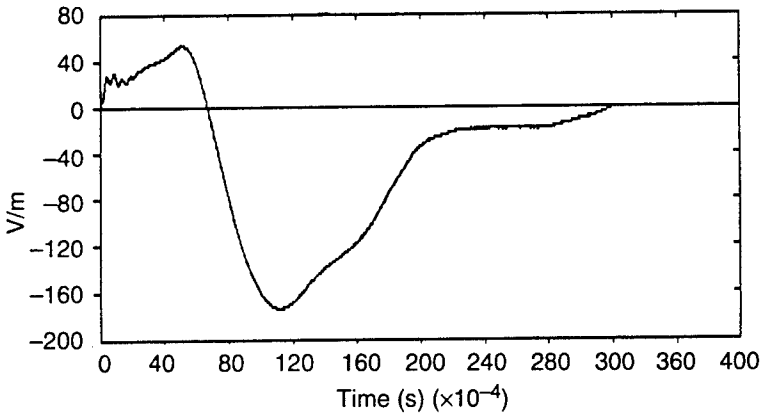

31, while the expected $1/r^3$ decay from the plate flight path is a factor of 28. Note that a $1/r^2$ decay from the coil would be a reduction factor close to one. Figure 15 represents the largest late-time *E*-field recorded; however, peak amplitudes greater than 10 kV/m were measured at locations closer to the plate. The dipole moment associated with I_p is difficult to quantify, but may be on the order of 10 kAm, which would produce an *E*-field amplitude consistent with the measured data. Based on the *H*-field measurement sensitivity, the wave impedance of the late-time signal is greater than 1 kΩ as would be expected in the near field of an electrically short dipole radiator.

The measured amplitude variations are not consistent with the launch coil as the source of this late-time *E*-field. Further, the measured signal has features that are related to the test point location, according to the plate velocity. This can be seen by comparing figure 16 to figure 15, where the location along the plate flight path (i.e., the *x*-coordinate) is the parameter of interest. If I_p is the source of the field, then the dominant features of the late-time signal should occur at the appropriate time when the plate passes the probe position. Based on the plate velocity, the late-time signal of figure 16 should occur about 1.5 ms before that of figure 15, and this is consistent with the measured data. Similarly the late-time signal of figure 12 should occur about 3.5 ms before that of figure 16 and about 2 ms before that of figure 15. At this location, (20,–28,10), the probe is close to the muzzle and should record a late-time signal at plate exit (i.e., 2 ms) that should decay as the plate moves further away. These trends are consistent with the measured data to within about 0.5 ms. The bipolar nature of the measured *E*-field can also be understood in terms of I_p, which is small near the plate front edge, but much larger and oppositely directed at the plate back edge. Thus the measured *E*-field reverses polarity as the plate passes the probe location and decays according to I_p. There is some variation in this part of the waveform, depending on probe position, as the signal will also decay as the plate moves away from the probe.

An estimate for the decay time of I_p can be obtained with an *RL*-circuit model for the eddy currents induced in the plate. The plate resistance, R_p, and inductance, L_p, depend only on the plate geometry and resistivity. The plate characteristic length, l_p, is 11.4 cm and the area normal to this length, A_p, is 6.45 cm^2. The resistivity of aluminum is 2.62×10^{-6} Ω-cm, so the plate resistance is estimated as

$$R_p = \frac{\rho_{Al} l_p}{A_p} = 4.64\ \mu\Omega\ . \tag{4}$$

The inductance of a rectangular plate can be readily calculated [8] as

$$L_p = 0.0021 l_p \left[\ln\left(\frac{2 l_p}{B_p + C_p} \right) + \frac{1}{2} - \ln(e) \right] \approx 0.0021 l_p \left[\ln\left(\frac{2 l_p}{B_p + C_p} \right) + \frac{1}{2} \right] = 28.6\ \text{nH}\ , \tag{5}$$

where $B_p = 10.2$ cm is the plate width and $C_p = 0.6$ cm is the plate thickness. Therefore the decay time is

$$\tau_d = \frac{L_p}{R_p} \approx 6.2 \text{ ms} , \tag{6}$$

which is consistent with the measured data. It is important to note that the plate is stopped at 15 ms, but the decay time to zero, based on the above estimate, is on the order of 30 ms. The late-time field peaks when the plate passes the probe position (i.e., from about 8 to 12 ms). The time to zero after this is difficult to measure but is typically more than 10 ms. Thus this signal cannot be a motional emf owing to the moving plate, and there are no anomalies in the measured data at 15 ms.

4. Conclusions

This report presents the EM field data available to date. Additional data for different values of I, and hence v_x, are required for a complete understanding of the EME in terms of these system parameters. Sufficient data are available for a basic understanding of the measured EME associated with the launch coil; however, the dipole model proposed to describe the late-time E-field requires more data as a function of v_x to be completely conclusive. This model would require a more detailed knowledge of I_p in order to produce numerical results for comparison. A reasonable model for the external launch coil would be a current filament approximation to the coil conductors that must include the feed cable and busbar connection. In this model the EM fields are quasi-static, so the transient characteristics of the EME are that of the coil current.

Several preliminary conclusions can be inferred from the empirical evidence. The early-time EME is magnetic with a wave impedance on the order of 10 mΩ. The source of this quasi-static EME is the launch coil current, where the spatial distribution would depend on the coil configuration/containment. That is, the amplitude of this EME would scale according to I and the spatial variation near the coil would depend on the distribution of field lines within the coil. This field distribution is changed when the plate is inserted and includes a contribution from the busbar connecting the top and bottom coils. Further away, the total fields decay as $1/r^2$, but the vector nature still depends on both the coil and feed cable configurations. The results indicate that larger scale systems would generate a magnetic EME that may be of concern for EME effects.

The late-time EME is electric with no measurable H-field, which implies a wave impedance >1 kΩ. This EME is quasi-static and would be directly proportional to the dipole moment associated with I_p. The late-time EME would then scale according to I_p rather than I, and experiments could be designed to confirm this dependence. The transient characteristics depend on v_x and the probe position with respect to the plate flight path. However, the bipolar nature and amplitude of this late-time waveform depends on the distribution of I_p over the plate. The decay time of this field is that of I_p and provides insight into the induced eddy currents in this plate. A better understanding of the induced plate current is required for a complete

model for this part of the EME associated with a launched plate. The empirical evidence indicates that I_p is the source of this late-time EME and that the spatial distribution varies as the inverse cube of the distance from the plate flight path. This electric EME is sufficient to disrupt sensitive electronics depending on the EM coupling efficiency to such equipment [9]. Additional data are required to further investigate the implications of these preliminary conclusions.

Acknowledgments

The authors would like to acknowledge the efforts of Chuck Hummer, Clint Hollandsworth, and Paul Berning in providing and operating the test bed for these measurements. The authors would also like to thank Ron Chase for his comprehensive technical review and for providing the decay time calculation.

References

1. M. Cowen, *Multistage Reconnection Gun*, PAT-APPL-7-034 354, Filed: 6 April 1987.

2. M. Cowen, M. M. Widner, E. C. Cnare, B. W. Duggin, R. J. Kaye, and J. R. Freeman, *Exploratory Development of the Reconnection Launcher, 1986–1990*, Proc. IEEE Trans. Magnetics **27**, no. 1, pp. 563–567 (January 1991).

3. C. R. Hummer and C. E. Hollandsworth, *Launching of Flat Plates With a Single Stage Reconnection Gun*, Proc. of the 8th IEEE International Pulsed Power Conference, IEEE Cat. No. 91CH3052-8, San Diego, CA, p. 789 (16–19 June 1991).

4. C. R. Hummer and C. E. Hollandsworth, *A Single-Stage Reconnection Gun*, U.S. Army Research Laboratory, ARL-TR-14 (November 1992).

5. M. L. Haberman, *EMI/EMC Issues Associated with Rail Guns*, Department of Defense, Electromagn. Compatib. Analysis Cent., ECAC-CR-93-086 (November 1993).

6. Y. M. Lee and B. T. Benwell, *Calibration Techniques and Procedures for Ground-Plane-Version Electric and Magnetic Field Sensors*, Harry Diamond Laboratories (now part of the U.S. Army Research Laboratory), HDL-TR-2159 (July 1989).

7. D. White, *A Handbook on EM Shielding Materials and Performance*, Don White Consultants, Inc. (1975).

8. F. W. Grover, *Inductance Calculations: Working Formulas and Tables*, D. Van Nostrand Co., Inc. (1946).

9. W. O. Coburn, E. Nguyen, R. J. Reyzer, and M. H. Mar, *High-Altitude Electromagnetic Pulse Survivability Assessment of the Harris RF-3200 Transceiver*, Harry Diamond Laboratories (now part of the U.S. Army Research Laboratory), HDL-SR-92-2 (September 1992).

Appendix A.—Electromagnetic Field Data

A set of the available electromagnetic field data is shown here for completeness. The test point location is included in the figure captions. In many cases, all three vector components of the field are measured and included in the figure. The magnetic field data (in amperes per meter) are shown in figures A-1 through A-9. The time scale is in 10^{-5} s, except figures A-9(a) and (b), where the time scale is in 10^{-4} s. The electric field data (in volts per meter) are shown in figures A-10 through A-14. The time scale is either 10^{-5} s (early-time data) or 10^{-4} s (late-time data).

Figure A-1. Measured H_z at location (0,0,23).

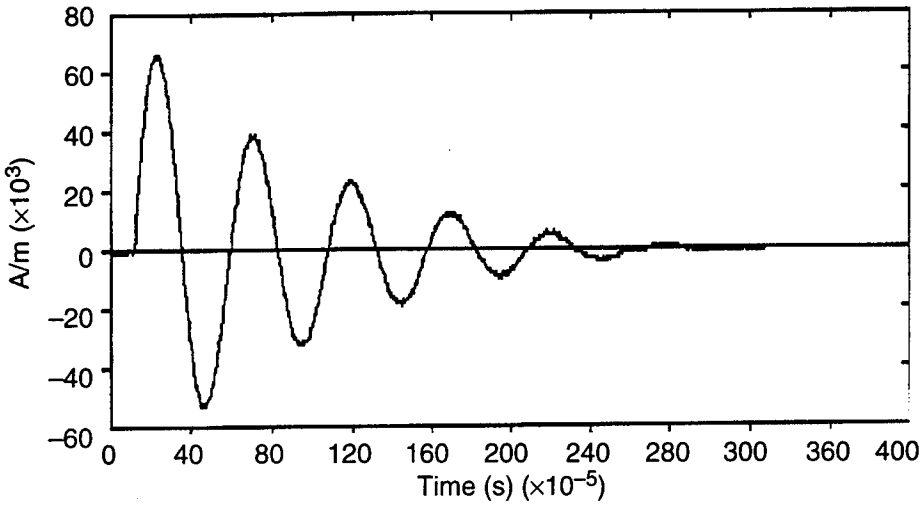

Figure A-2. Measured H_z at location (–8,8, 23).

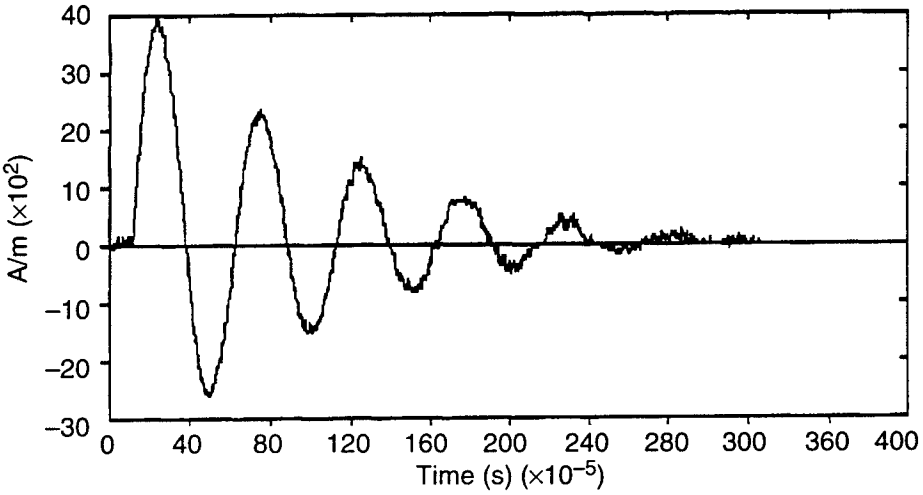

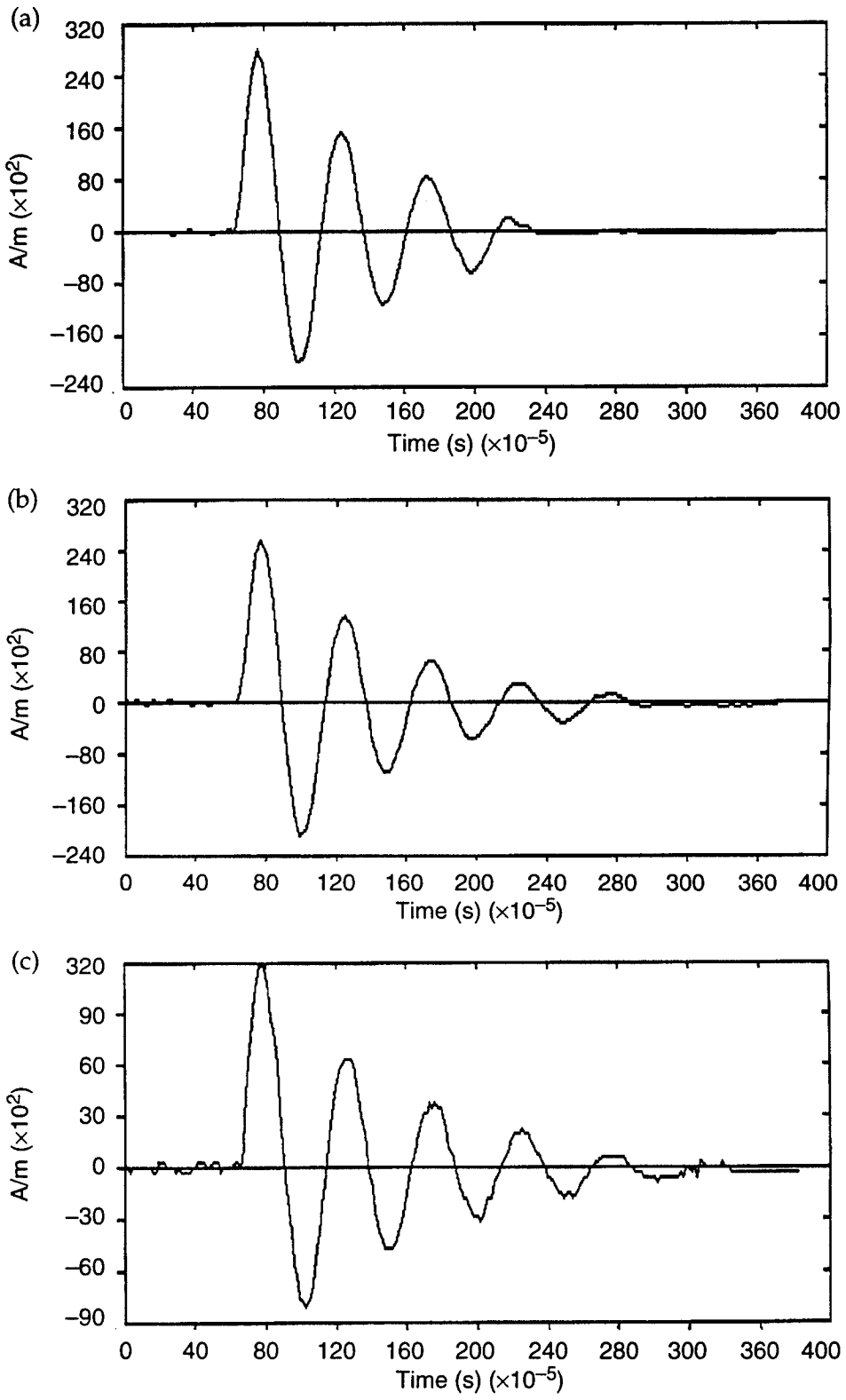

Figure A-3. Measured (a) H_x at location (0,28,10), (b) H_y at location (0,28,10), and (c) H_z at location (0,18,10).

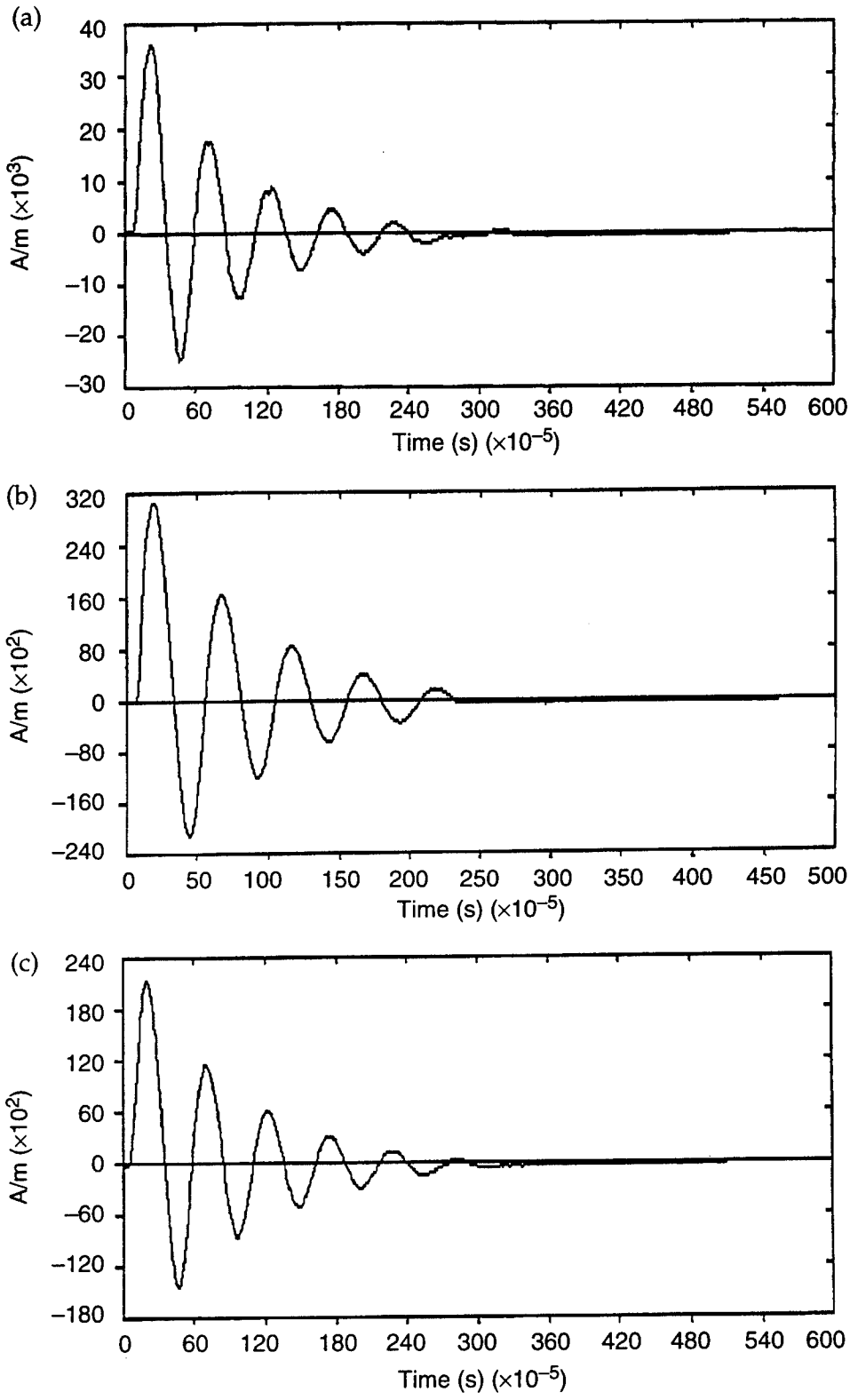

Figure A-4. Measured (a) H_x at location (0,–28,0), (b) H_y at location (0,–28,0), and (c) H_z at location (0,–28,0).

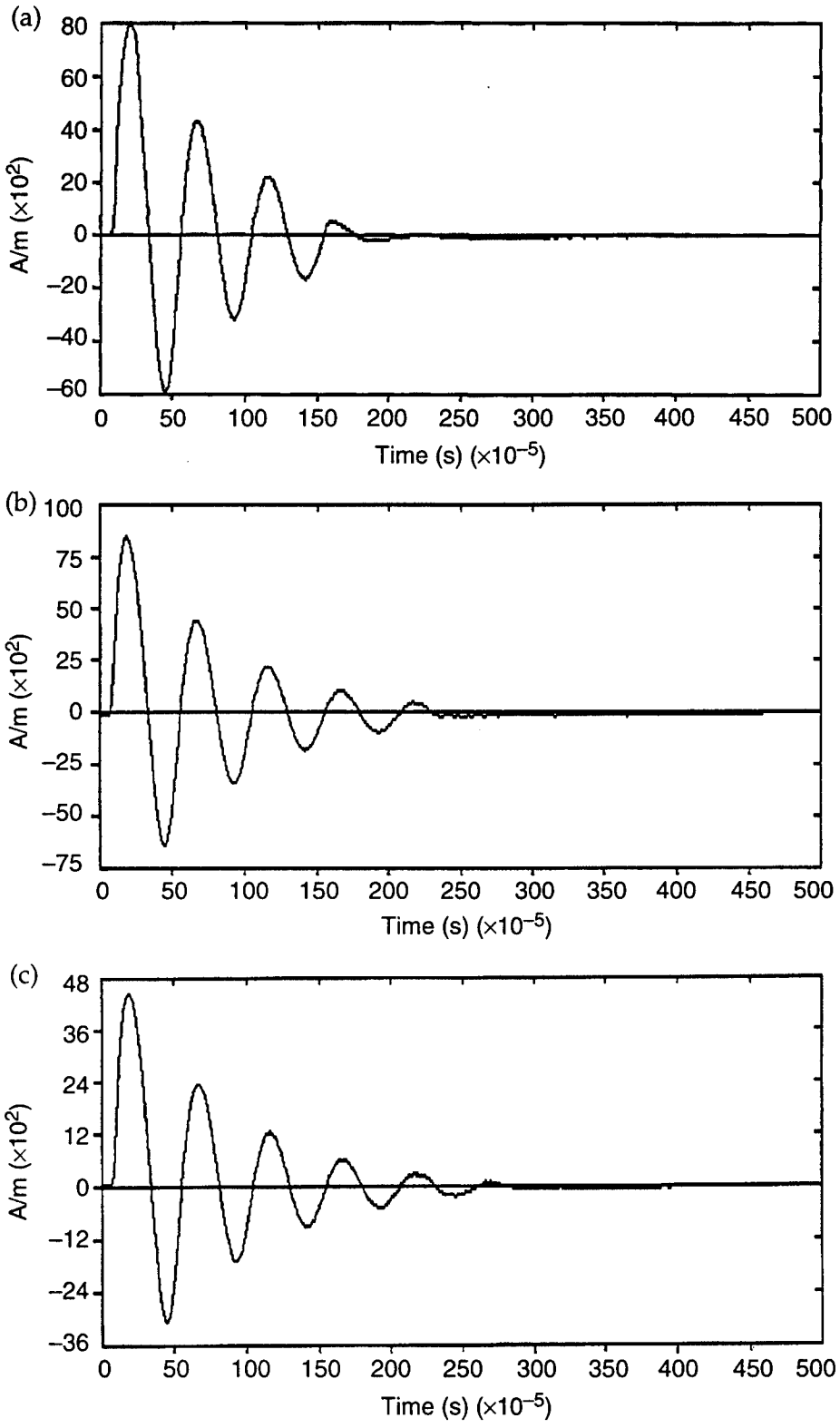

Figure A-5. Measured (a) H_x at location (0,–56,0), (b) H_y at location (0,–56,0), and (c) H_z at location (0,–56,0).

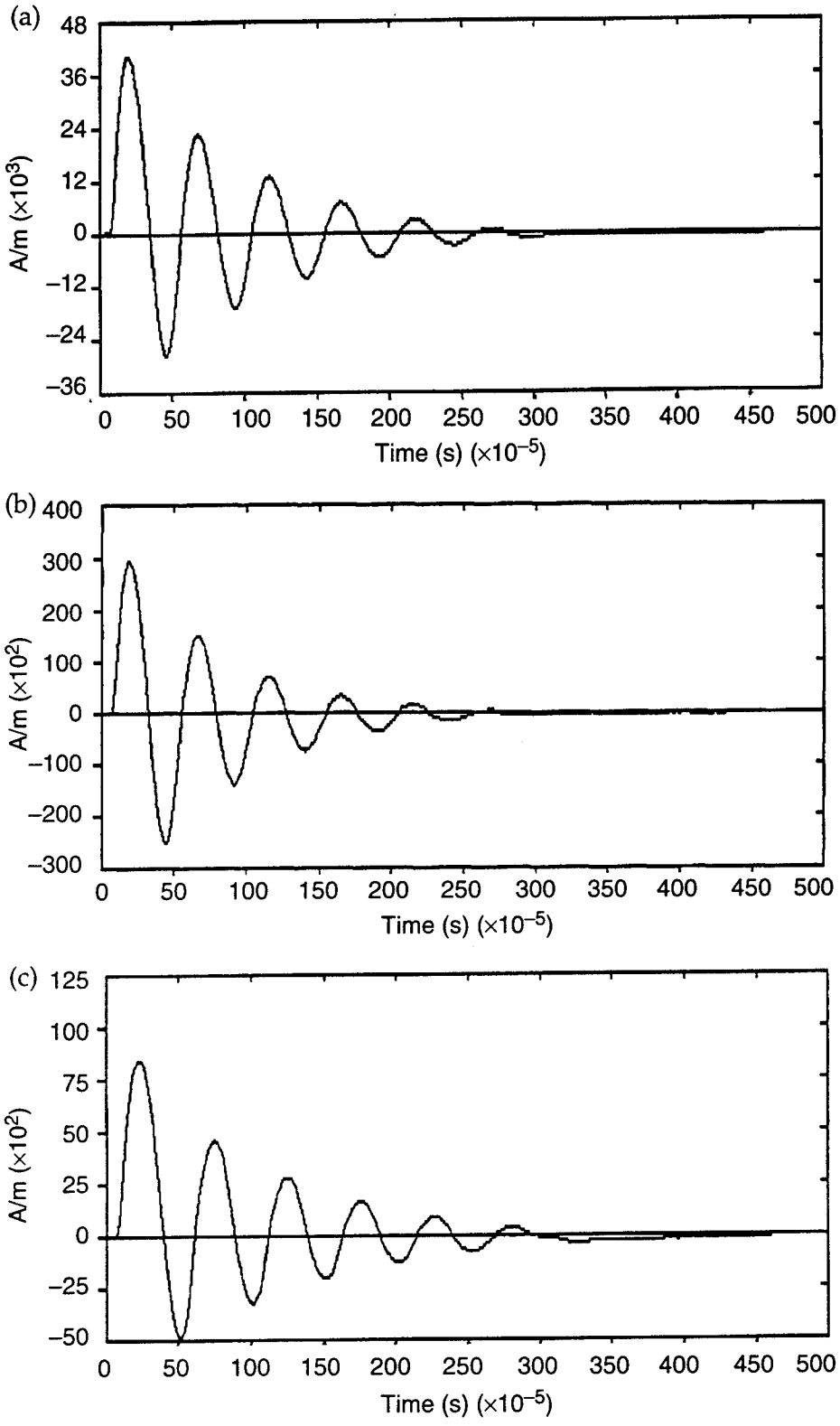

Figure A-6. Measured (a) H_x at location (15,0,15), (b) H_y at location (15,0,15), and (c) H_z at location (15,0,10).

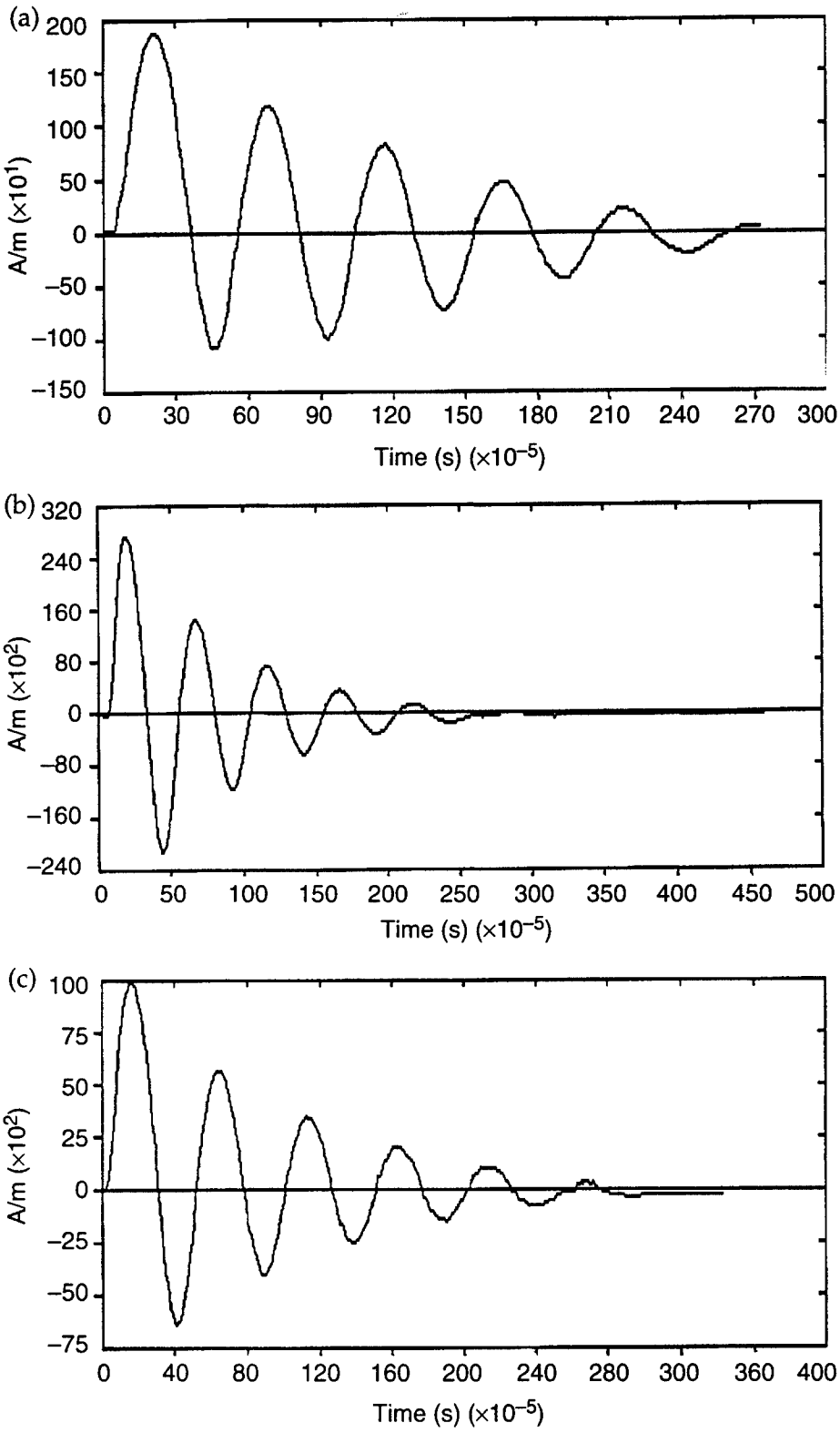

Figure A-7. Measured (a) H_x at location (15,0,28), (b) H_y at location (15,0,28), and (c) H_z at location (15,0,280).

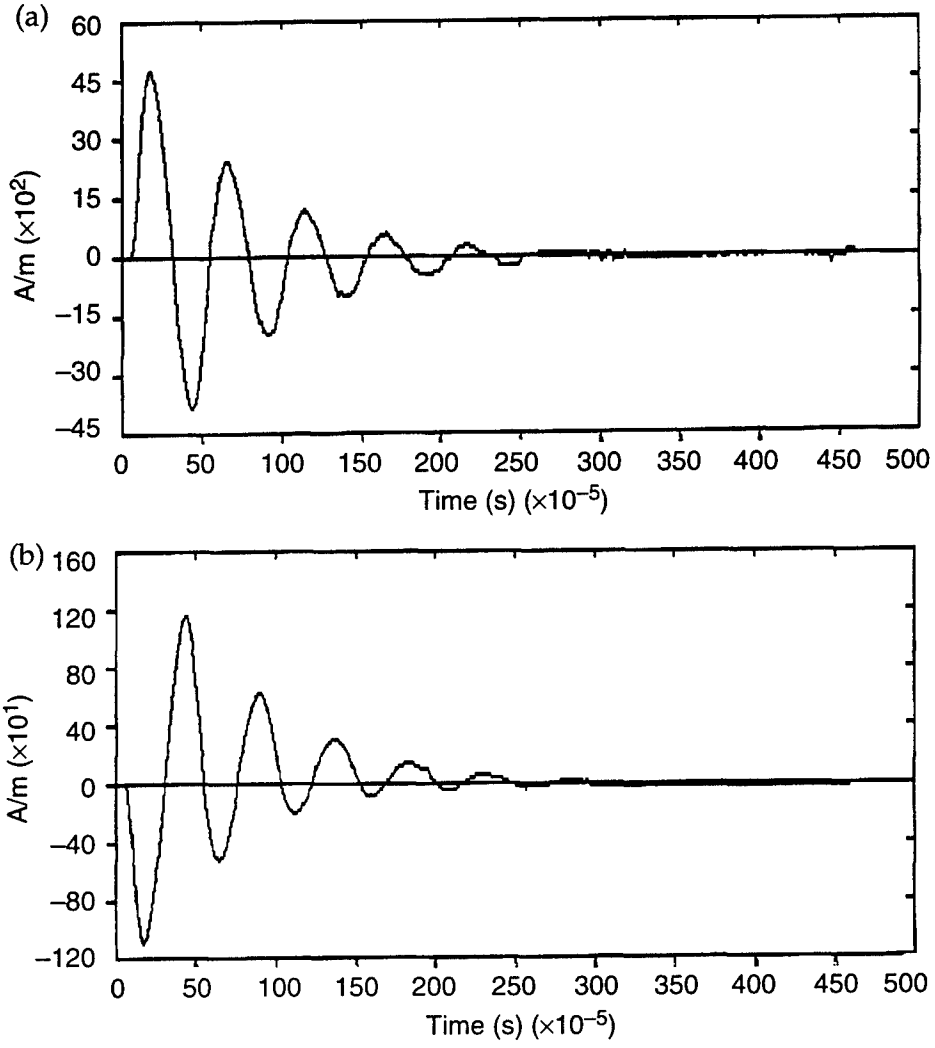

Figure A-8. Measured (a) H_x at location (28,13,30) and (b) H_z at location (28,13,30).

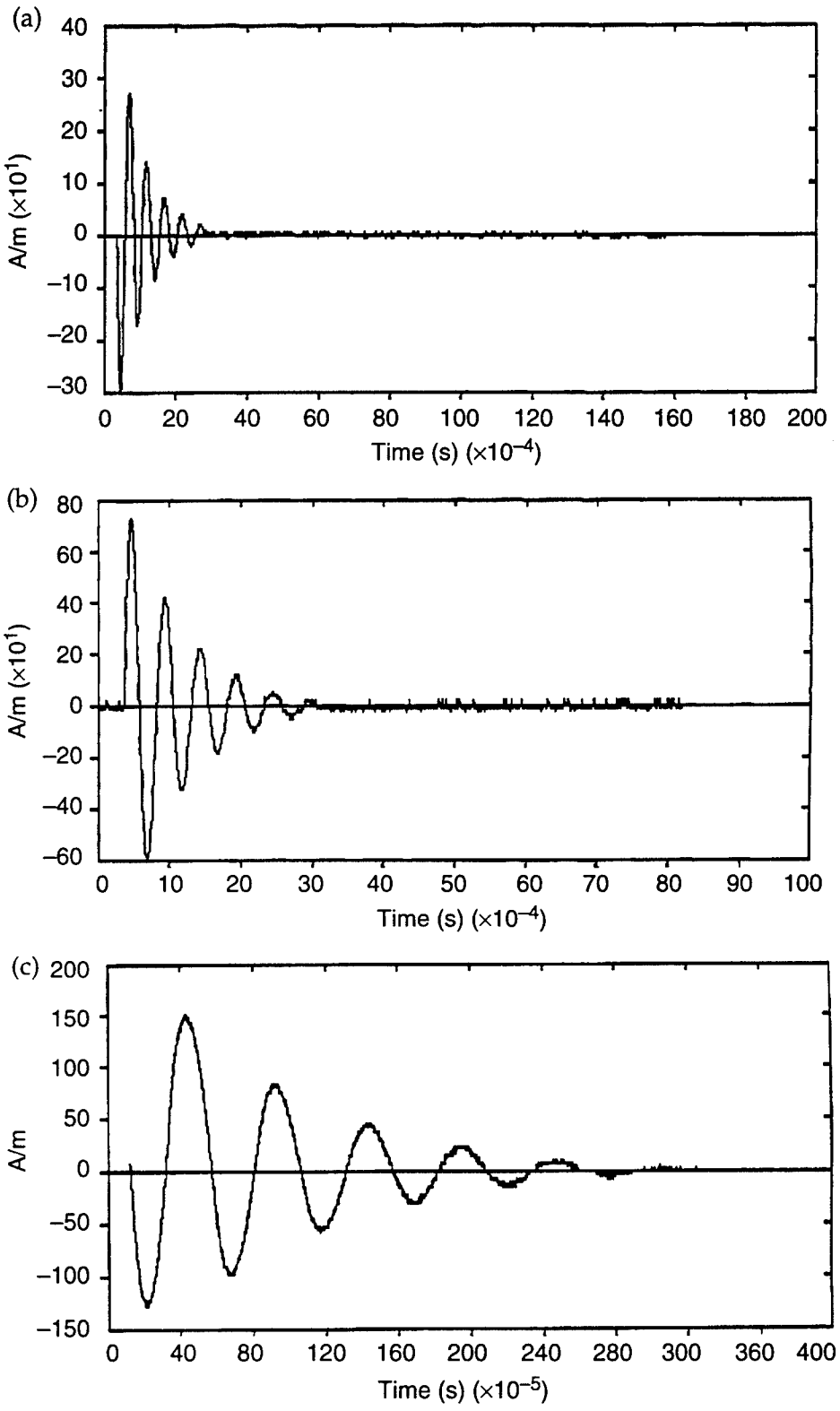

Figure A-9. Measured (a) H_x at location (84,13,43), (b) H_y at location (84,13,43), and (c) H_z at location (84,13,43).

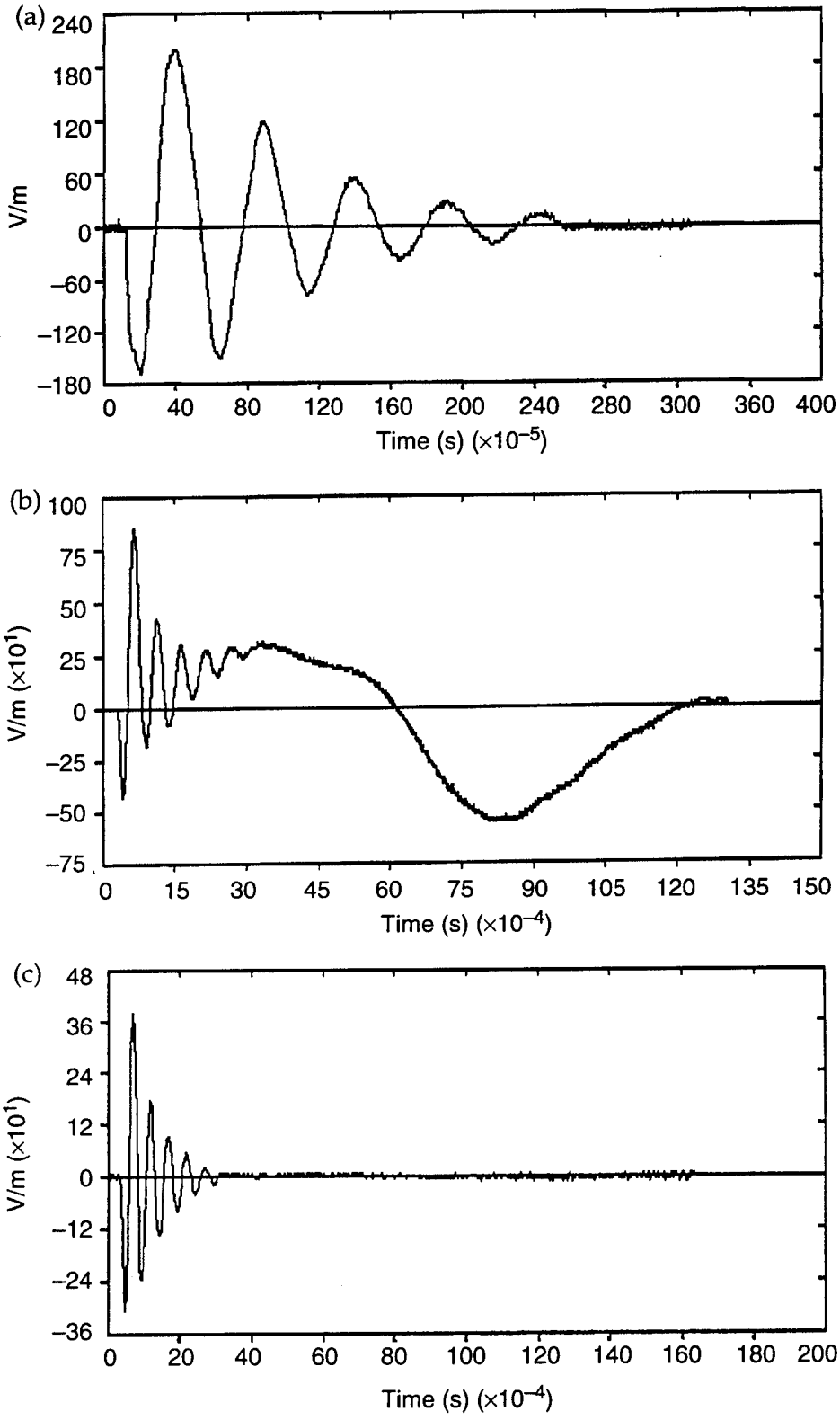

Figure A-10. Measured (a) E_x at location (20,–28,10), (b) E_y at location (20,–28,10), and (c) E_z at location (20,–28,10).

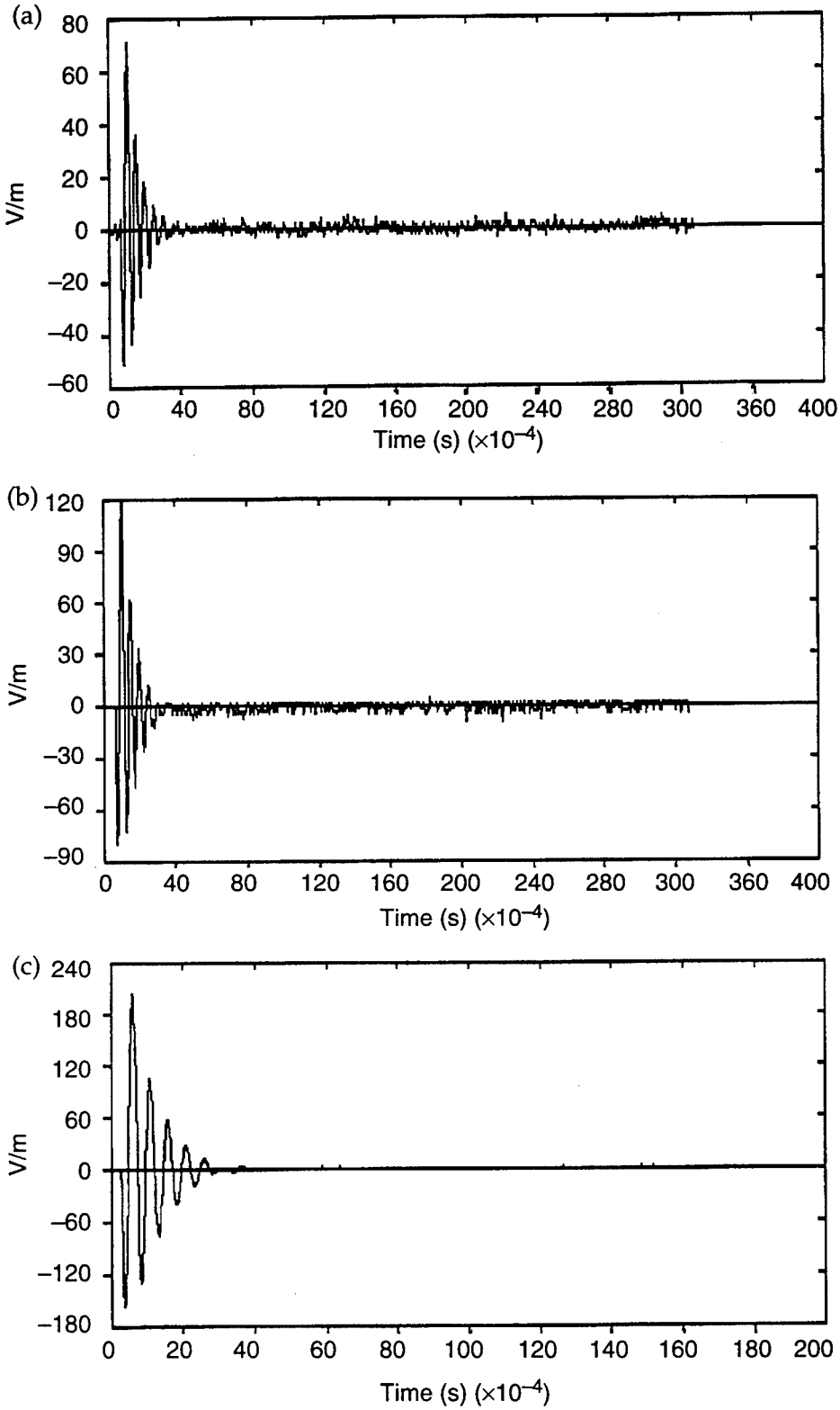

Figure A-11. Measured (a) E_x at location (20,–56,10), (b) E_y at location (20,–56,10), and (c) E_z at location (20,–56,10).

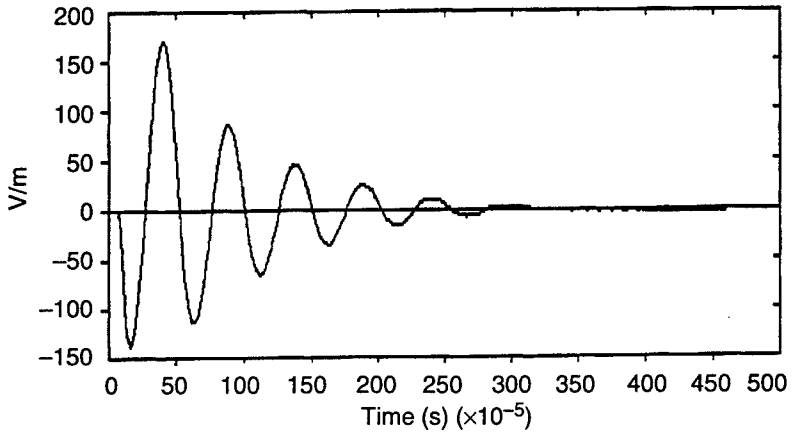

Figure A-12. Measured E_x at location (33,–20,0).

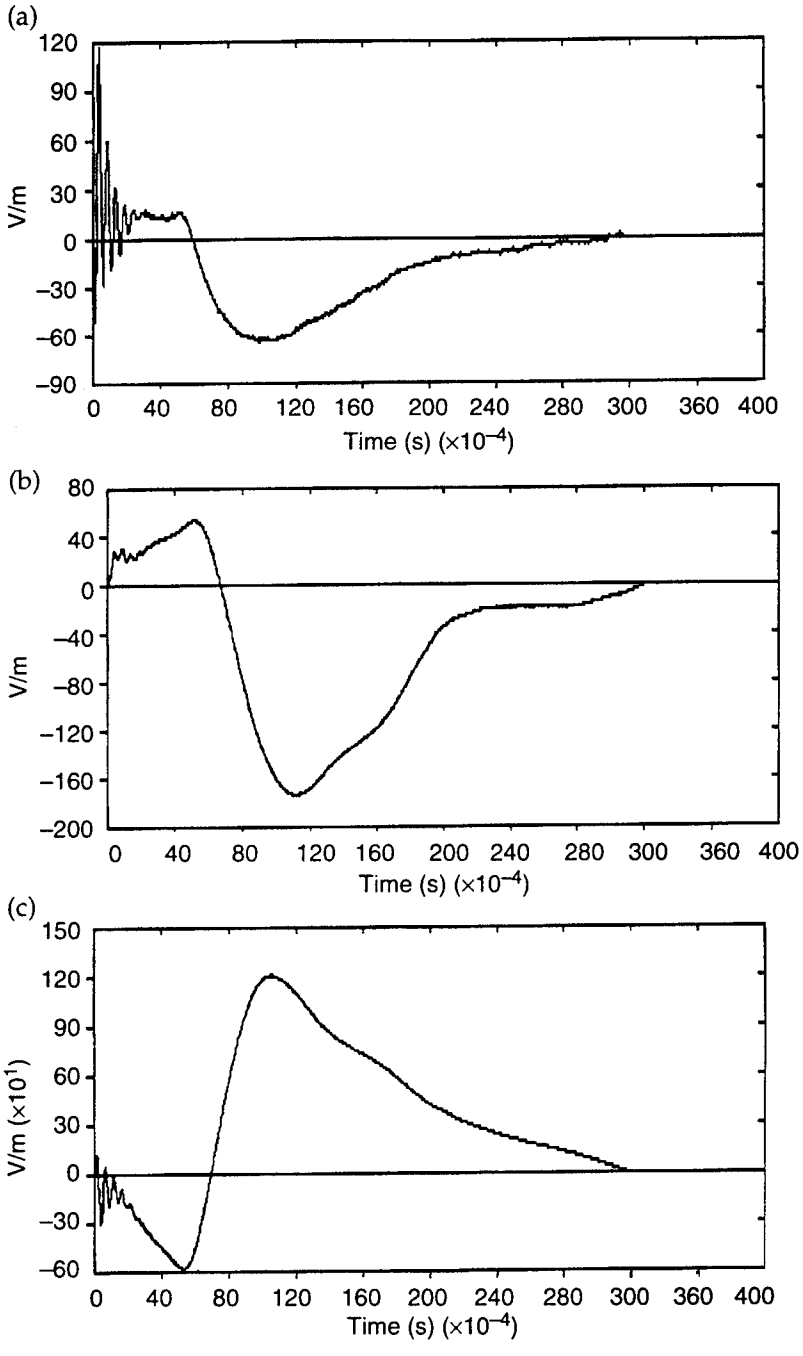

Figure A-13. Measured (a) E_x at location (36,0,28) and (b) E_y at location (38,0,28).

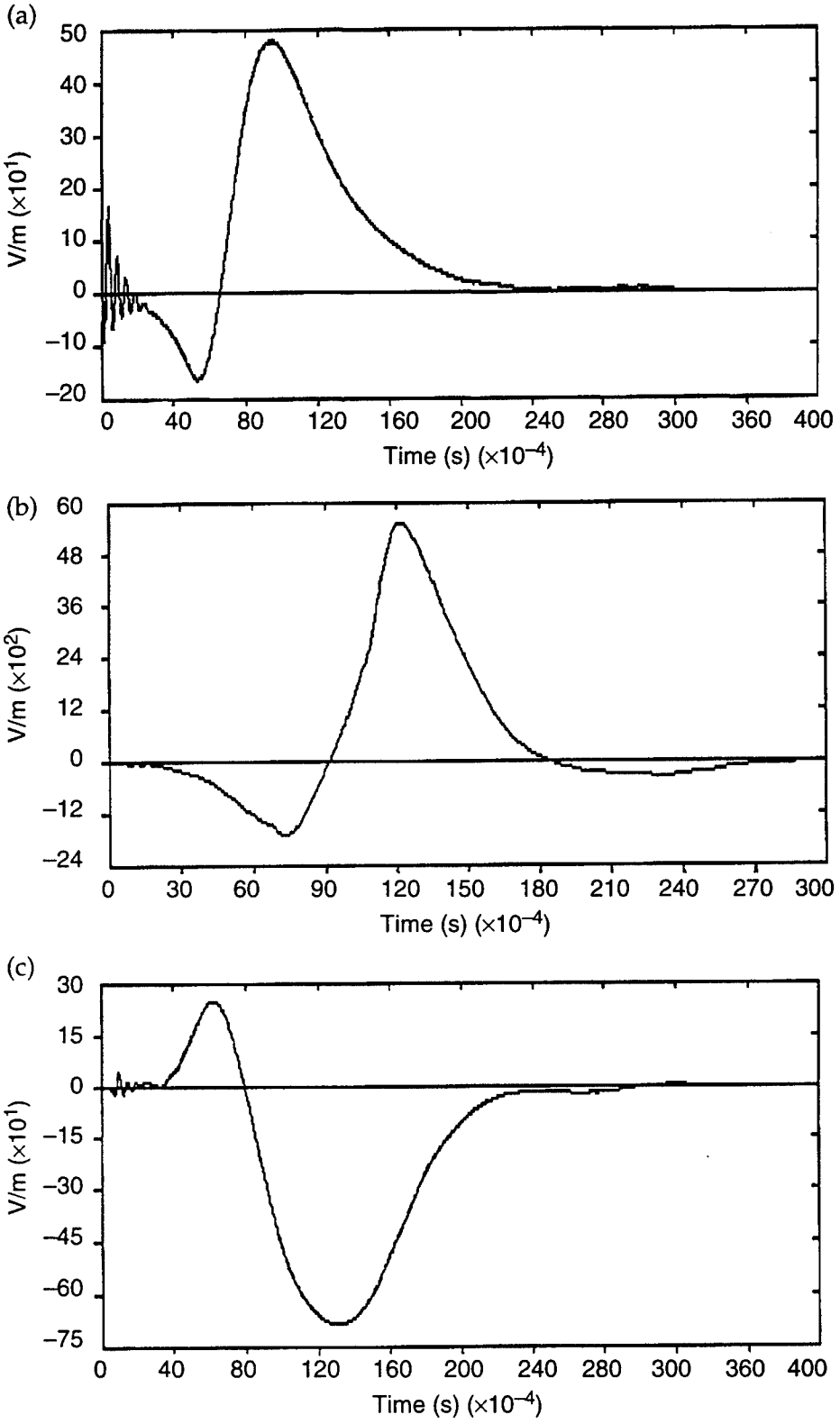

Figure A-14. Measured (a) E_x at location (41,20,8), (b) E_y at location (41,20,8) and (c) E_z at location (41,20,8).

Distribution

Admnstr
Defns Techl Info Ctr
Attn DTIC-DDA (2 copies)
Cameron Sta Bldg 5
Alexandria VA 22304-6145

Dir
Defns Intllgnc Agcy
Attn RTS-2A Techl Lib
Washington DC 20301

Defns Nuc Agcy
Attn RAES Elect Syst Techlgy Div
Attn RAST Electromagnetic Applctn Div
Attn TITL Tech Lib
6801 Telegraph Rd
Alexandria VA 22310-3398

Defs Nuc Agency
Office of Techl Applications
Attn D R Lewis
Alexandria VA 22310

Commander
Atmospheric Sci Lab
Attn STEWS-NE J Meason
White Sands Missile Range NM 88002-5180

Ofc of the Assist Secy of the Army for Rsrch
Dev & Acqstn
Attn SARD-TR Dr R Chait
Room 3E476 The Pentagon
Washington DC 20310-0103

Cmdr
US Army ARDEC
Attn AMSTA-AR-CCL-D W Williams
Attn SMCAR-AEC-IE N Svendsen
Bldg 65 N
Picatinny Arsenal NJ 07806-5000

US Army AVRDEC
Attn AMSAT-R-EFM P Haselbauer
4300 Goodfellow Blvd
ST Louis MO 63120-1798

US Army BRDEC
Attn SATB-FGE J Ferrick
Attn SATB-FGE T Childers
FT Belvoir VA 22060-5606

Cmdr
US Army Matl Cmnd
Attn AMCAM-CN
5001 Eisenhower Ave
Alexandria VA 22333-0001

Dir
US Army Mis Cmnd (USAMICOM)
Attn AMSMI-RD-CS-R Documents
Redstone Arsenal AL 35898-5400

Cmdr
US Army MRDEC
Attn AMSMI-RD-ST-CM J Vandier
Huntsville AL 35898-5240

US Army Natick RDEC
Attn SATNC-SUSD-SHD A Murphy
Kansas Stret
Natick MA 01760-5018

Commander
US Army Nuc & Chem Agcy
Attn MONA-NU R Pfeffer
7150 Heller Loop Rd Ste 101
Springfield VA 22150

Cmdr
US Army TARDEC
Attn AMSTA-ZT G Baker
Warren MI 48397-5000

Commander
US Army TECOM
Attn STERT-TE-E J Knaur
Redstone Technical Test Center
Huntsville AL 35898-8052

US Army TECOM Techl Dir Ofc
Attn AMSTE-TC-D R Bell
Aberdeen Proving Ground MD 21005

Nav Rsrch Lab
Attn Code 4820 Techl Info Div
4555 Overlook Ave SW
Washington DC 20375-5000

Commander
Nav Surfc Weapons Ctr
Attn Code E231 Techl Lib
Dahlgren VA 22448-5020

Distribution

Nav Warfare Ctr
Attn Code OZT T Conway
Lakehurst NJ 08733

Dir Air Force Armament Directorate
Attn WL/MNAA S Federle
101 W Eglin Blvd. Ste 346A
Eglin AFB FL 32542-6810

Natl Inst of Stand & Techlgy
Attn V Ulbrecht Rsrch Info Ctr
Rm E01 Bldg 101
Gaithersburg MD 20899

DoD Joint Spectrum Center
Attn CA J Word (3 copies)
120 Worthing Basin
Annapolis MD 21401

US Army Rsrch Lab
Attn AMSRL-WT-PB Chf
Attn AMSRL-WT-WB Chf
Attn AMSRL-WT-WC Chf
Attn AMSRL-WT-WD Chf
Aberdeen Proving Ground MD 21005

US Army Rsrch Lab
Attn AMSRL-OP-SD-TA Mail & Records Mgmt
Attn AMSRL-OP-SD-TL Tech Library (3 copies)
Attn AMSRL-OP-SD-TP Tech Pub
Attn AMSRL-SS-F Chf
Attn AMSRL-SS-S Chf
Attn AMSRL-WT-N Chf
Attn AMSRL-WT-NB Chf
Attn AMSRL-WT-ND C Le (10 copies)
Attn AMSRL-WT-ND Chf
Attn AMSRL-WT-ND W O Coburn
Attn AMSRL-WT-NE Chf
Attn AMSRL-WT-NF Chf
Attn AMSRL-WT-NG Chf
Attn AMSRL-WT-NH Chf
Attn AMSRL-WT-NJ Chf
Attn AMSRL-WT-N Sr Rsrch Scntst
Attn AMSRL-WT-ND J Latess